Exploring the effect of complex hierarchic microstructure of quenched and partitioned martensitic stainless steels on their high cycle fatigue behaviour

Sierra-Soraluce, A.; Li, G.; Santofimia, M. J.; Molina-Aldareguia, J. M.; Smith, A.; Muratori, M.; Sabirov, I.

Important note
To cite this publication, please use the final published version (if applicable).
Please check the document version above.

Exploring the effect of complex hierarchic microstructure of quenched and partitioned martensitic stainless steels on their high cycle fatigue behaviour

A. Sierra-Soraluce [a], G. Li [b], M.J. Santofimia [b], J.M. Molina-Aldareguia [c,a], A. Smith [d], M. Muratori [e], I. Sabirov [a,*]

[a] IMDEA Materials Institute, Eric Kandel, 2, Getafe 28906, Spain
[b] Department of Materials Science and Engineering, Delft University of Technology, Mekelweg 2, CD Delft 2628, the Netherlands
[c] Department of Mechanical Engineering, Universidad Politécnica de Madrid, José Gutierréz Abascal, 2, Madrid 28006, Spain
[d] RINA Consulting - Centro Sviluppo Materiali SpA, Castel Romano 100, Rome 00128, Italy
[e] Acerinox Europa S.A.U., Acerinox Europa, Los Barrios 11379, Spain

ARTICLE INFO

ABSTRACT

Recent studies have demonstrated the viability of quenching and partitioning (Q&P) treatment for processing martensitic stainless steels showing an improved balance of high strength and sufficient ductility. However, to date, the fatigue behaviour of these materials has not been explored. This study examines the effect of their complex hierarchic microstructure on high cycle fatigue performance. Three steels with different alloying element contents underwent Q&P processing, resulting in multiphase microstructures rich in retained austenite. High cycle fatigue tests and analysis of fatigue fracture surfaces were performed using SEM and EBSD techniques. The results indicate satisfactory high cycle fatigue performance in Q&P treated martensitic stainless steels, surpassing traditional counterparts. Fatigue cracks predominantly form and propagate along martensite packet and block boundaries, while prior austenite grain boundaries and MnS inclusions have minimal influence on fatigue crack formation and growth. Microplastic deformation at the fatigue crack tip enhances local KAM values and triggers localized transformation of retained austenite grains. It is hypothesized that the developed Q&P treated martensitic stainless steels exhibit improved resistance to low cycle fatigue.

1. Introduction

Automotive engineers continue to look for ways to make vehicles lighter, cut fuel consumption and associated emissions, and improve performance and handling. For example, it is estimated that emissions decrease 6.9 % for every 10 % of weight removed. So, engineers are turning to aluminium, magnesium and titanium alloys, composites, and advanced high-strength steels (AHSSs). Martensitic stainless steels are ideally suited for structural components and assemblies, satisfying the requirements of high strength, toughness and corrosion resistance. New developments in welding and thermal processing, coupled with increased demands for high strength lightweight structures, are positioning martensitic stainless steels as a cost effective alternative to conventional lightweighting materials [1]. One of the main drawbacks for the use of martensitic stainless steels for automotive applications has been their modest formability [1]. Introducing metastable retained austenite into the microstructure of martensitic steels typically improves

their strength-ductility balance and formability due to the transformation induced plasticity (TRIP) effect [2,3].

There are different strategies for manufacturing martensitic steels containing retained austenite. One of the most recent approaches, the so-called quenching and partitioning (Q&P) process, was proposed by Speer and colleagues in 2003 [4]. It is a multi-step thermal processing route. First, after full austenitization or intercritical annealing, the steel is quenched to a suitable pre-determined quenching temperature (QT) below the martensite start (M_s) but above the martensite finish (M_f) temperatures to form a pre-defined amount of martensite. Second, the steel is either held at this QT or brought to a higher partitioning temperature (PT), where the untransformed austenite is carbon-enriched through carbon depletion of the supersaturated martensite [5,6]. In this way, a complex microstructure formed by metastable retained austenite and martensite is obtained after final quenching to room temperature. The concept of Q&P process has been well elaborated for carbon steels, and numerous research and review articles can be found in

---

the current literature [7–9]. It has been demonstrated that the Q&P process can be successfully used to improve mechanical properties of carbon steels [7–9]. However, very few works have been done on the Q&P processing of martensitic stainless steels with a focus on microstructure and tensile properties [10–15]. Similar to carbon steels, martensitic microstructures with high fractions of retained austenite showing improved strength-ductility balance can be generated in these materials. Therefore, the Q&P treated martensitic stainless steels look attractive for commercial applications. However, their application-related properties have not yet been studied.

Fatigue resistance is one of the most important application-related properties of materials developed for automotive applications. It is essential to understand the cyclic behaviour of these materials to ensure their good performance in service. Several reports have shown a beneficial effect of retained austenite on the high cycle fatigue life of AHSSs [16,17] including Q&P treated carbon steels [18–21]. The stability of retained austenite plays an important role in their fatigue performance, and AHSSs with higher austenite stability exhibit better fatigue performance [17,18]. The microstructure of the Q&P treated steels and fatigue testing parameters significantly influence the fatigue life and mechanisms governing fatigue behaviour [19–21]. The transformation of retained austenite delays fatigue crack growth due to the crack closure effect [22]. Overall, this is a highly complex topic, and the effect of retained austenite on the high cycle fatigue resistance of AHSSs is an active area of research. There is still much that is not fully understood about the mechanisms that govern the influence of retained austenite on high cycle fatigue performance. Moreover, the fatigue properties of the Q&P processed martensitic stainless steels have never been investigated. The main objective of this study is to explore the high cycle fatigue performance of Q&P treated martensitic stainless steels and study the influence of their complex hierarchical microstructure on fatigue behaviour.

2. Materials and experimental procedures

2.1. Materials and processing

Three martensitic stainless steels with varying chemical compositions were selected for this study. The first alloy has a chemical composition of an AISI 410 grade. The second alloy represents an AISI 420 grade, and has a slightly higher Cr content. The third alloy is the AISI 420 grade with increased Mn content and microalloyed by Ti and Nb. Table 1 presents the chemical compositions of these alloys.

The steels were cast, hot-rolled and cold rolled to a final thickness of 1.5 mm. After cold rolling, a skin pass was given to all sheets to improve flatness. This was carried out by first heating the sheets to 100 °C for less than one minute, followed by applying the skin pass. Sheets having a length of 250 mm and a width of 200 mm were cut for further Q&P processing. The relatively low surface area of the sheets allows minimizing temperature gradients across the sheet resulting in homogeneous microstructure. All sheets were equipped with a K-type thermocouple at the centre (half-length and mid-width) to control temperature.

The applied Q&P heat treatment parameters are listed in Table 2. They were selected based on the outcomes of our recent work [15], where we investigated the effect of Q&P treatment parameters on the microstructure of the given steels. The Q&P treatments were performed using two furnaces in all cases. The first furnace was used for austenitisation at 1100 °C for 15 min. Austenitization at this temperature

Table 1
Chemical composition of the studied martensitic stainless steels (wt. %).

Alloy	C	Cr	Mn	Si	Ni	Al	N	Nb	Ti
410	0.2	12.5	0.7	0.35	0.2	0.01	0.03	–	–
420	0.3	13	0.7	0.35	0.2	0.01	0.03	–	–
420ma	0.3	13	3.0	0.35	0.2	0.01	0.03	0.05	0.05

Table 2
The Q&P treatment parameters applied to the studied martensitic stainless steels.

Alloy	Quenching T [°C]	Partitioning T [°C]	Partitioning time [min]
AISI 410	160	450	5
AISI 420	99	450	5
AISI 420ma	30	450	5

enables full dissolution of (Fe,Cr)C [23], homogenization of alloying elements in the microstructure, and retains nanoscale complex (Ti, Nb)C in 420ma alloy [24]. A second high-power furnace was used for stabilising at the quench temperature and the subsequent partitioning treatment. The thermal profile revealed that the heating rate to the austenitisation temperature was around 6–9 °C/s (depending on the sample). For cooling to the quench temperature, and final cooling at the end of the cycle, natural air cooling was used. The initial cooling rates were as high as 8 °C/s during cooling to the quench temperature, and reduced to a minimum value of 0.6 °C/s as the quench temperature was approached. The heating rate for the partitioning step was between 1 and 2.4 °C/s. For final cooling, initial cooling rates were around 2 °C/s and reduced to 0.5 °C/s close to room temperature, which are well above the critical cooling rates for martensitic stainless steels.

2.2. Microstructural characterization

Quantitative microstructural characterization of the Q&P treated sheets was performed through electron backscatter diffraction (EBSD) analysis. Specimens were ground and polished to a mirror-like surface applying standard metallographic techniques with final polishing using colloidal silica suspension (OPS). The EBSD studies were performed using an APREO 2S LoVac equipped with an Oxford Instruments Symmetry S2 EBSD detector controlled by the AZtec Oxford Instruments Nanoanalysis (version 5.0) software. The data were acquired at an accelerating voltage of 20 kV, a working distance of 13 mm, a tilt angle of 70°, and a step size of 50 nm. The orientation data were post-processed using HKL Post-processing Oxford Instruments Nanotechnology (version 5.12) software and TSL Data analysis version 8.0 software. The volume fractions of tempered martensite, fresh martensite and retained austenite were determined by a two-step partitioning procedure [25]. In this procedure, retained austenite and martensite are separated in the first step (Fig. 1a). The iron fcc phase exclusively consists of retained austenite, while the iron bcc contains tempered martensite and fresh martensite. In the second step, fresh martensite (FM) and tempered martensite (TM) are separated using the grain average image quality (GAIQ) criterion (Fig. 1b) which is directly correlated to the sharpness of the Kikuchi pattern. The fresh martensite formed during the final quench derivates from retained austenite that was not sufficiently stabilized during the partitioning step. Therefore, fresh martensite demonstrates lower GAIQ values compared to tempered martensite due to higher lattice distortions caused by a higher carbon content. The threshold GAIQ value is selected based on the distribution of GAIQ values in the map and their grain size. Furthermore, fresh martensite should be located close to retained austenite clusters and/or between tempered martensite laths, and it should be smaller in size and rounder in shape than tempered martensite. Additionally, fresh martensite has low quality on the band contrast map. This was used as another criterion to validate the selected GAIQ threshold value. It should be noted that a combination of various characterization techniques (such as EBSD, XRD, TEM and magnetometry) is required to gain a comprehensive insight into the volume fraction of retained austenite in Q&P treated steels [26]. For this particular study, we opted for the EBSD technique as it aligns better with the objectives of this work. While XRD and magnetometry measurements provide information from large areas
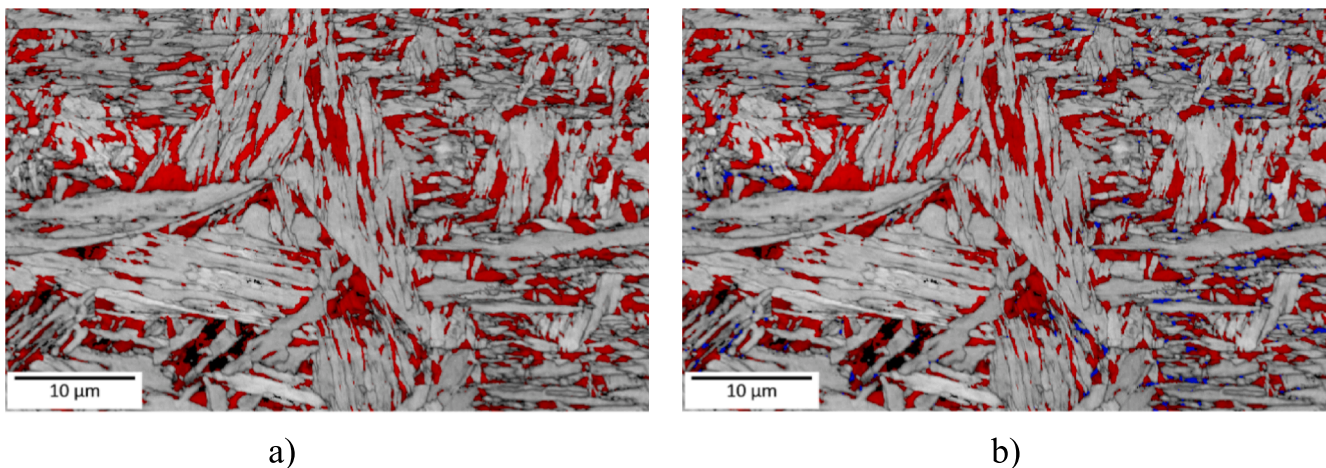
Fig. 1. A typical EBSD phase map of 420ma sample with identified microstructural constituents: a) in the first step, retained austenite (RA) in the martensitic matrix is detected; b) in the second step, fresh martensite (FM) and tempered martensite (TM) are discriminated. FM is in blue, RA is in red, and TM is the matrix. (For interpretation of the references to colour in this figure legend, the reader is referred to the web version of this article.)

and volumes, respectively, the TEM technique yields data from a very small area not being able to provide representative information. From the obtained EBSD data, we can extract quantitative information about the volume fractions and grain size of individual microconstituents, as well as local misorientation maps. The retained austenite grain size was calculated as an average grain diameter. The microstructure was observed on the plane perpendicular to the sample transverse direction (the RD–ND plane). The MTEX package for Matlab, and specifically, a routine developed by T. Nyyssonen and colleagues [27] was used to reconstruct the prior austenite grain boundaries and perform quantitative analysis of the microstructural features of the martensitic matrix (martensite packet size and martensite block size).

To study nanoscale complex carbides formed in the 420ma alloy, transmission electron microscopy (TEM) studies were carried out using a FEG S/TEM (Talos F200X, FEI) operated at an accelerating voltage of 200 kV. Thin foils were prepared on a TenuPol 5 (Struers®) by twin-jet electropolishing with 10% perchloric acid in acetic acid at 15 °C at an operating voltage of 40 V. TEM imaging was carried out in bright-field (BF) and high-angle annular dark field (HAADF) modes. Elemental mapping was carried out using energy dispersive spectroscopy (EDS) detector SuperX (4 detectors) from FEI & Bruker, integrated in the TEM.

Fracture surfaces of the broken fatigue specimens were carefully studied in the scanning electron microscope APREO 2S LoVac operating at an accelerating voltage of 20 kV. EDS analysis was performed using Oxford Instruments Ultim Max 40 detector to identify MnS inclusions when necessary.

2.3. Tensile and fatigue testing

Standard tensile samples having a gauge length of 50 mm and gauge width of 12.5 mm were machined from the Q&P treated sheets. Tensile tests were carried out at room temperature according to the ASTM 8-EM

standard [28].

Specimens for fatigue testing were also machined from the Q&P processed sheets. The geometry of samples is presented in Fig. 2. The surface of the specimens was carefully prepared using standard metallographic techniques to remove the superficial defects that could have been induced during the machining process and the oxide layer formed during the Q&P process, as well as to improve the surface quality. After sample preparation, the high cycle fatigue tests were performed in pull-pull stress-controlled mode using sinusoidal-waveform cyclic loading. The experiments were carried out at room temperature using an INSTRON 8802 servohydraulic fatigue testing system according to ISO 1099 standard [29]. The stress ratio R was 0.1, and the load frequency f was 50 Hz. The stress amplitude σ_a -values were in the range of 260 – 490 MPa. The number of cycles to failure was recorded, and the S-N curves (Wohler curves) were plotted. At least 14 samples were tested per each material. The fatigue limit σ_f was estimated from the obtained Wohler curves.

3. Results

3.1. Microstructure of the Q&P treated martensitic stainless steels

Typical EBSD band contrast maps overlaid by corresponding inverse pole figure (IPF) maps for retained austenite grains and corresponding kernel average misorientation (KAM) maps are shown in Fig. 3a-c. There is no pronounced crystallographic texture of retained austenite (Fig. 3a-c). Its volume fraction tends to increase from 9.7 % in 410 alloy to 15.7 % in 420 alloy to 18.7 % in the 420 ma alloy (Table 3). This observation can be related to the increasing content of austenite-stabilizing alloying elements, carbon and manganese (Table 1) [3,30]. In all studied materials, the retained austenite grains are homogeneously distributed over the martensitic matrix. Two morphologies of retained austenite are
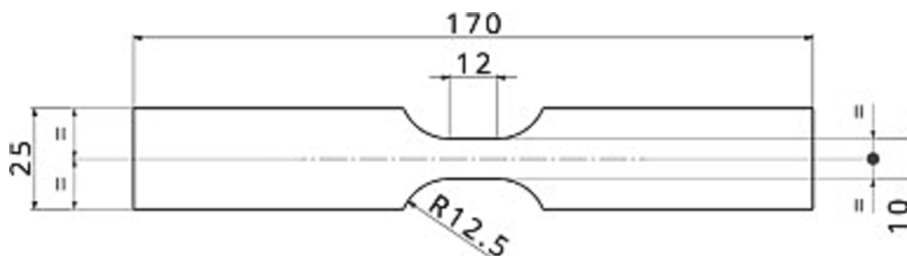
Fig. 2. Geometry of samples used for high cycle fatigue testing.
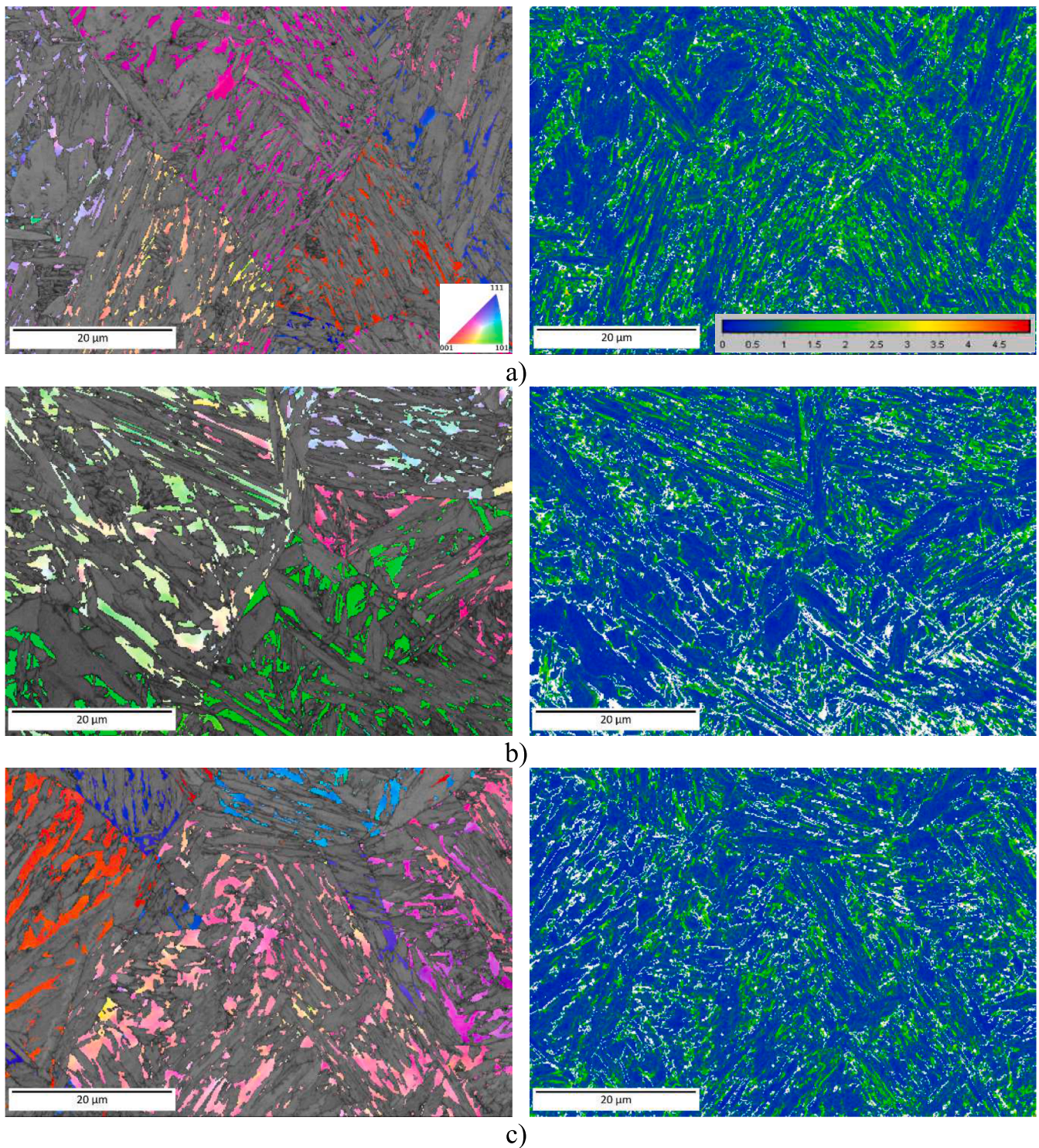
Fig. 3. a-c) Typical microstructures of the Q&P treated martensitic stainless steels: a) 410; b) 420; c) 420ma. Left: EBSD band contrast map overlaid by retained austenite IPF map; Right: KAM map of the corresponding area; d) A fragment of EBSD band contrast map illustrating prior austenite grain (PAG) boundaries, martensite packet boundaries and block boundaries (in the central grain) in the Q&P treated 420ma alloy.

observed: relatively coarse blocky retained austenite having equiaxed shape with a grain size of ≥ 1 μm and finer elongated interlath-lamellar retained austenite located between martensite laths. There is no significant effect of chemistry on the average grain size of retained austenite, which is presented in form of equivalent circular diameter (Table 4). It should be noted that in Q&P treated steels, film-type retained austenite, typically having a thickness of ~ 10 nm, is also present [31]. However,

the EBSD technique cannot resolve it due to pixel size limitations.

The matrix microstructure in all materials exhibits a typical lath martensite structure which is schematically shown in Fig. 3d. Prior austenite grains are divided into several packets which in turn consist of blocks. The interior of martensite laths has nearly zero local misorientations, whereas the martensite lath boundaries show higher local misorientations of 1…1.5° (Fig. 3a-c). The non-indexed pixels (white
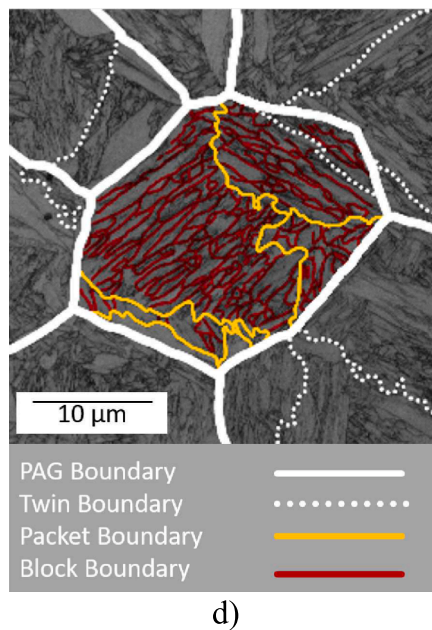
Fig. 3. (*continued*).

Table 3
Microstructural constituents identified using EBSD analysis and their local volume fractions.

Alloy	Retained austenite (FCC) [%]	Martensite (BCC) [%]			Non-indexed [%]
		BCC phase total	Tempered martensite	Fresh martensite	
410	9.7	79.5	75.1	4.4	10.8
420	15.7	69.5	63.4	6.1	14.8
420ma	18.7	66.6	60.6	6.0	14.7

Table 4
Size of the microstructural constituents determined using EBSD analysis.

Alloy	Retained austenite Grain size [μm]	Martensite			Fresh martensite size [μm]	Prior austenite grain size [μm]
		Tempered martensitic matrix				
		Packet size [μm]	Block size [μm]	Lath width [μm]		
410	0.7 ± 0.3	21.6 ± 11.7	3.8 ± 1.5	1.2 ± 1.2	0.50 ± 0.04	38.3 ± 2.9
420	0.9 ± 0.6	11.9 ± 4.3	3.5 ± 0.9	0.9 ± 0.8	0.40 ± 0.08	29.4 ± 15.7
420ma	0.8 ± 0.6	8.4 ± 1.9	2.7 ± 0.9	0.9 ± 0.8	0.50 ± 0.20	20.4 ± 7.0

pixels on KAM maps) correspond to prior austenite grain/packet/block boundaries or fresh martensite. Ultra-fine non-indexed areas on the KAM maps (white pixel areas, Fig. 3a-c) correspond to fresh martensite, which could not be indexed due to high lattice distortion [25,32]. Its volume fraction tends to slightly increase with the increasing content of alloying elements.

The average sizes of the microstructural constituents measured by a line interception method are listed in Table 4. It is seen that the microalloying by Nb and Ti noticeably reduces prior austenite grain size from 38.3 μm in alloy 410 down to 20.4 μm in alloy 420ma. The finer prior austenite grains result in finer martensite packet size (Table 4) [33]. This microstructural refinement in alloy 420 ma is related to the formation of nanoscale NbC and TiC particles in the grade 420ma (Fig. 4b), which are homogeneously distributed over the microstructure

of the Q&P treated alloy 420 ma. They have a spherical shape with average sizes of 67.4 ± 1 4.7 nm and 44.1 ± 18.5 nm, respectively (Fig. 4b). The NbC precipitates tend to decorate TiC nanoprecipitates. These complex (Ti,Nb)C nanocarbides effectively pin grain boundaries thus refining the microstructure during thermo-mechanical processing and austenitization [34]. Also, the finer prior austenite grains could increase the volume fraction of retained austenite in the Q&P treated 420ma alloy (Table 3). It was recently demonstrated that finer prior austenite grains result in a faster and more efficient carbon partitioning process than coarser microstructures through the formation of smaller and more homogeneously distributed phases during the first quench [35]. In all Q&P treated steels, elongated nanoscale Fe_3C were detected. Their length was 50…250 nm and width was 10…15 nm. They were homogeneously distributed over the microstructure. TEM images (Fig. 4a) clearly illustrates their presence in the interior of martensite lath of the 410 alloy.

Carbon content in retained austenite plays important role as it determines its stability [2,3]. Estimation of carbon content in the Q&P treated martensitic stainless steel is a challenging task, as it was already demonstrated in [13]. Different empirical equations used to calculate carbon content in martensitic stainless steels based on the measurements of lattice parameter lead to different results. Therefore, in this work, we estimated the carbon content using the measured volume fractions of retained austenite and martensite from the full partitioning assumption, where all carbon is assumed to accumulate in the austenite. It sets an upper limit for the carbon concentration in austenite. The procedure is described in [36]. The estimated carbon content was 2.01 wt.% in 410 alloy, 1.89 wt.% in 420 alloy and 1.49 wt.% in 420ma alloy.

3.2. Tensile properties of the Q&P treated martensitic stainless steels

Table 5 summarizes the tensile properties measured for the studied steel grades. All alloys exhibit a high strength with an ultimate tensile strength (UTS) value above 1200 MPa and sufficient tensile ductility with total elongation values above 10%. The optimal combination of tensile strength and ductility is shown by the 420 alloy. Despite having a higher Mn content and the presence of complex (Ti, Nb)C nanocarbides, the 420ma alloy shows tensile properties similar to those of the 420 alloy. Earlier studies have shown that the strengthening effect of complex (Ti, Nb)C nanocarbides is very low [15,37]. Additionally, the
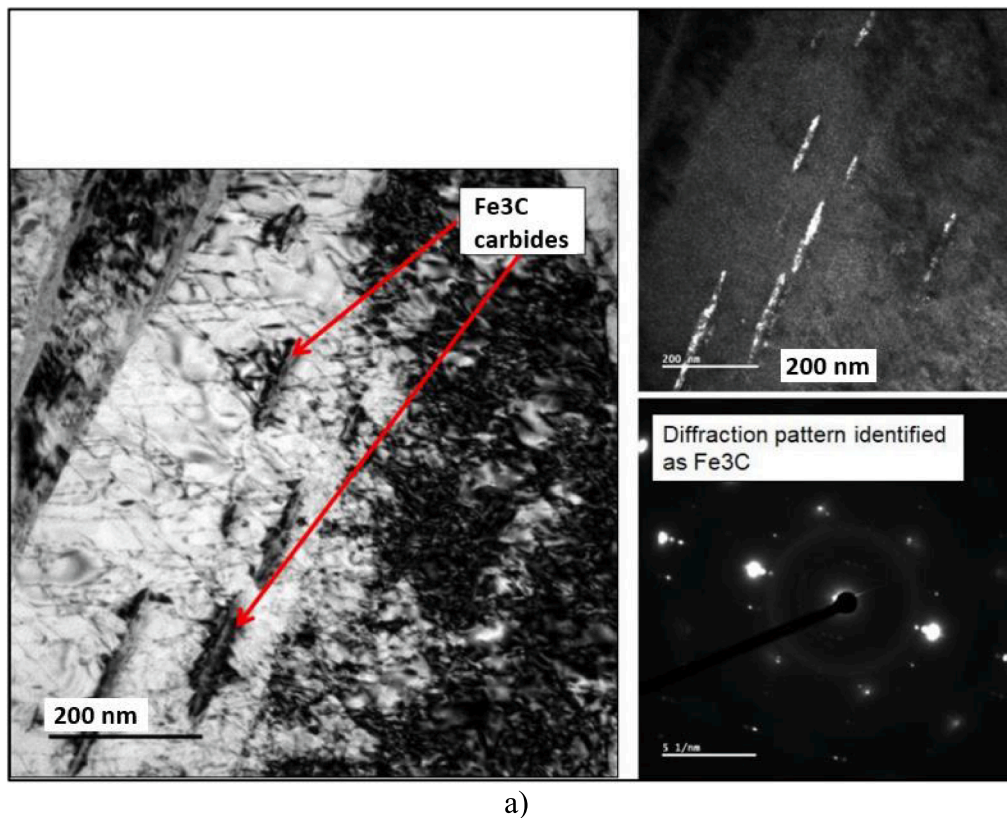
Fig. 4. A) appearance of Fe₃C nanoscale carbides in the Q&P treated 410 steel; b) appearance of complex (Ti, Nb)C nanocarbides in the microstructure of the Q&P treated 420ma steel.

420ma alloy shows a higher volume fraction of retained austenite and, particularly, blocky retained austenite compared to the 420 alloy (Fig. 3b-c, Table 4), which provides an additional softening effect [38].

3.3. Cyclic behaviour of the Q&P treated martensitic stainless steels

Fig. 5 illustrates the S–N curves obtained from high cycle fatigue testing of the studied materials. At stress amplitudes higher than 440 MPa, the experimental points for all tested steels overlap. The number of cycles, that the steels can endure before failure, tends to increase with decreasing stress amplitude. For the 410ma steel, the S–N curve becomes horizontal at the stress amplitude $\sigma_a = 270$ MPa after 10^7 cycles, which is referred to as the material's fatigue limit σ_f [39]. Alloy 410 exhibits a better fatigue limit and can withstand more than 10^7 cycles at the stress amplitude $\sigma_a = 300$ MPa. The Q&P treated alloy 420 shows the best fatigue performance with a fatigue limit of 320 MPa. It should be noted that a few samples showed a dramatically reduced fatigue life for a given stress amplitude. An example is shown for alloy 410, where one sample could withstand more than 1.2×10^7 cycles at a stress amplitude of 300 MPa, whereas another sample failed after 1.6×10^5 cycles (the latter marked by a red cross on Fig. 5). Such points were excluded from further consideration because the SEM analysis of the fatigue fracture surfaces revealed fatigue crack initiation at surface rolling defects.

3.4. Fatigue fractography analysis

The fatigue fracture surfaces of the broken samples were thoroughly analysed. As is well known, there are three stages of fatigue failure: crack initiation, stable crack propagation and unstable crack growth followed by rupture [40]. The areas corresponding to each stage could be easily recognized in all analysed samples. In the vast majority of samples, regardless of the alloy and applied stress amplitude, the fatigue cracks formed at the sample surface by transgranular cracking (i.e. through prior austenite grains), and the morphology of their fatigue fracture surfaces looked very similar. Fig. 6 presents SEM images of the fatigue crack initiation and propagation areas of the 410 alloy tested with $\sigma_a = 320$ MPa (289263 cycles to failure). The fatigue crack initiation area is marked by a white arrow (Fig. 6a). Its size is approximately 30 μm (Fig. 6b). Fig. 7 illustrates the only case of fatigue crack formation via intergranular cracking observed in the 420ma alloy tested with the stress amplitude $\sigma_a = 300$ MPa (62619 cycles to failure). Grain boundaries can be easily seen, and grain size matches well with the prior austenite grain size of the 420ma alloy.

Fatigue crack propagation occurs also predominantly in transgranular mode. Fatigue crack striations are observed over the fatigue crack propagation area of all samples. Their typical appearance is illustrated on Fig. 6c and Fig. 8a. Such striations represent local crack-growth increments and have been hypothesized to occur via a mechanism of opening and blunting of the crack tip on loading, followed by resharpening of the tip on unloading [41]. Fig. 8b shows a spot of local crack propagation along prior austenite grain boundaries observed on the surface of the 420 alloy tested with $\sigma_a = 325$ MPa (644000 cycles to failure). It should be noted that the size of such spots does not exceed 100 μm and their surface fraction is negligibly low. MnS inclusions debonded from the martensitic matrix can be clearly seen over the crack propagation areas of all tested samples (Fig. 8a). It should be noted that one sample (420ma alloy tested with $\sigma_a = 460$ MPa) showed a MnS inclusion on the fatigue crack initiation area (Fig. 9a,b). This was also confirmed by the outcomes of the EDS analysis (Fig. 9c), which ruled out a possibility of fatigue crack formation at a corrosion pit, as no oxygen was detected.

b)
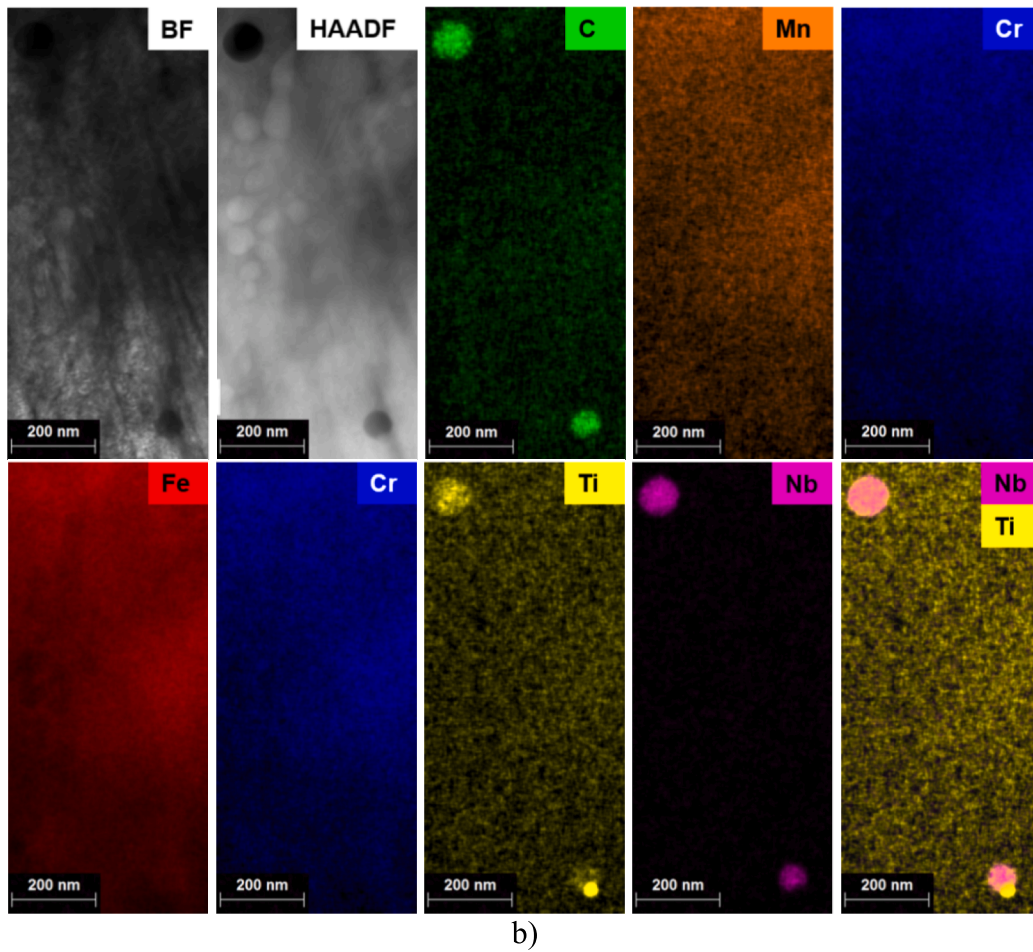
Fig. 4. (*continued*).

Table 5

Data from tensile and fatigue testing of the Q&P treated martensitic stainless steels.

Material	Tensile testing			Fatigue testing		
	$\sigma_{0.2}$ [MPa]	σ_{UTS} [MPa]	ε [%]	σ_f [MPa]	σ_f /σ_{UTS}	σ_{max} /σ_{UTS}
410	936 ± 3	1276 ± 20	11.4 ± 2.4	300	0.24	0.54
420	1089 ± 11	1472 ± 43	14.0 ± 1.3	320	0.22	0.48
420ma	1082 ± 46	1451 ± 62	10.3 ± 0.7	270	0.19	0.41

4. Discussion

4.1. Fatigue performance of the Q&P treated martensitic stainless steels

The analysis of the S–N curves (Fig. 5) indicates that the best fatigue limit is shown by alloy 420 (320 MPa) followed by alloy 410 (300 MPa) and then by alloy 420ma (270 MPa). However, another important parameter to be considered is the ratio of fatigue limit to ultimate tensile strength (σ_f /σ_{UTS}) which is proportional to σ_{max}/σ_{UTS}–ratio when the material is tested with the same *R*. Based on this consideration, the highest σ_f /σ_{UTS} -ratio is demonstrated by alloy 410 (0.24) followed by alloy 420 (0.22) and then by alloy 420ma (0.19) (Table 5). The materials under study are characterized by a highly complex multiphase microstructure that includes a tempered (softened) martensitic matrix with a hierarchical substructure, fresh (hard) martensite and retained austenite
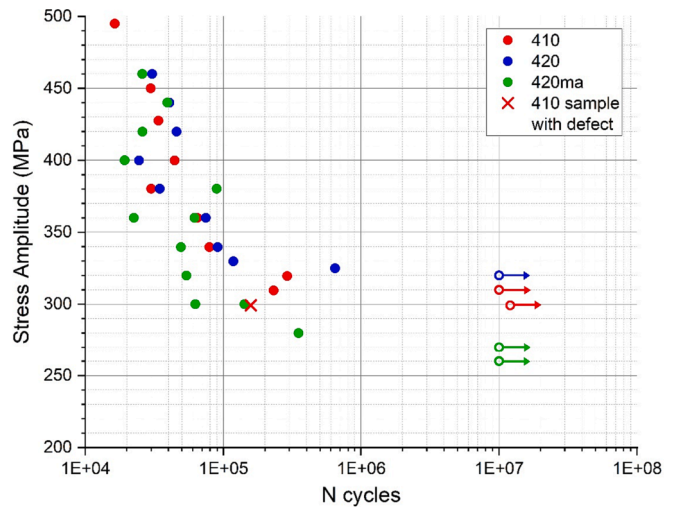
Fig. 5. The *S-N* curves obtained from high cycle fatigue testing of the Q&P-treated martensitic stainless steels. One sample with fatigue crack initiated at surface rolling defects is marked by a cross (x).

grains (Section 3.1). However, the volume fractions of the microstructural constituents, as well as their morphology, size, and mechanical stability of retained austenite grains vary across the studied materials. This variability makes it very challenging to reliably understand the individual effects of each microstructural constituent on the high cycle
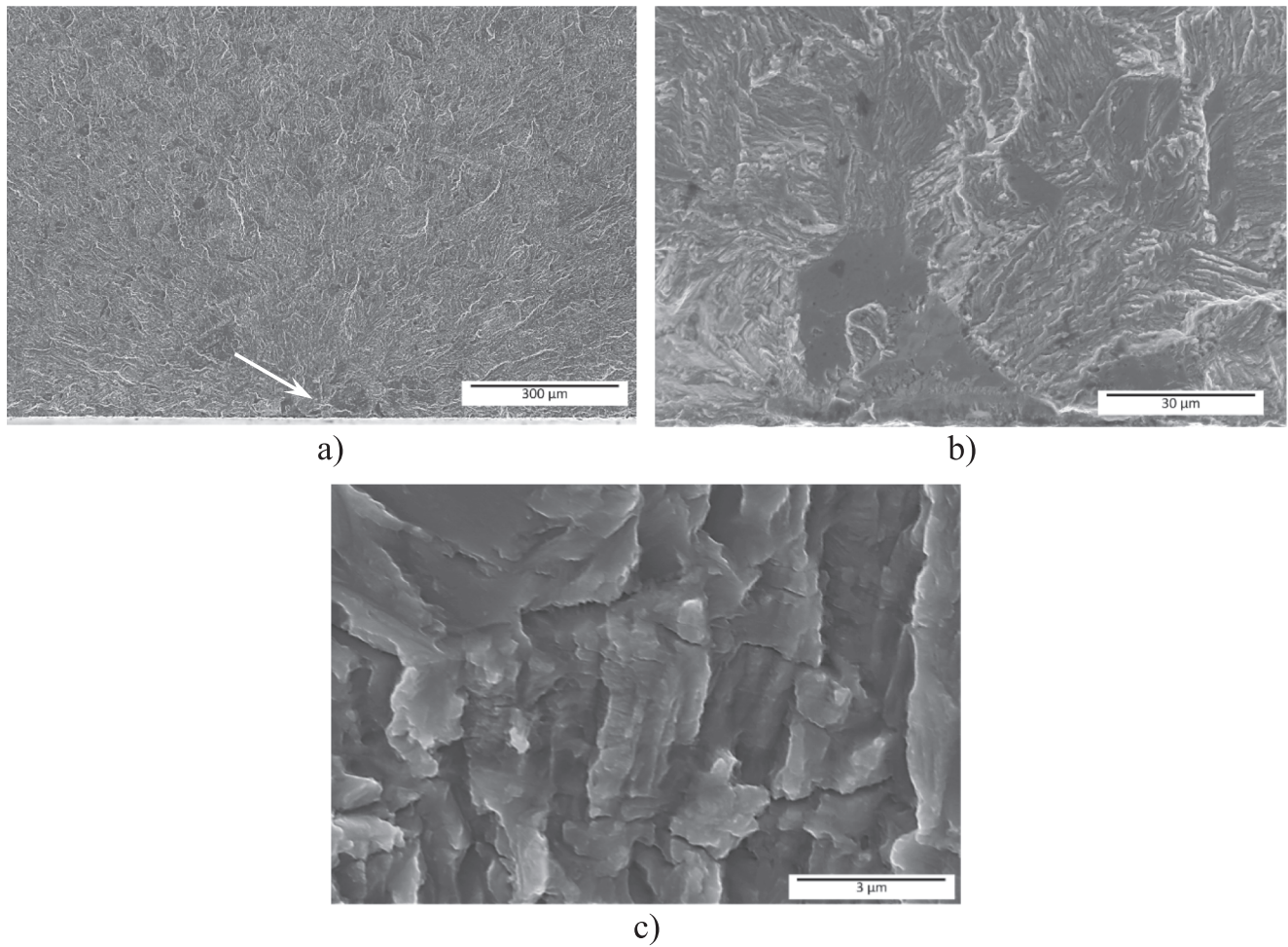
Fig. 6. SEM images of fatigue fracture surface shown by 410 alloy tested with $\sigma_a = 320$ MPa (289263 cycles to failure): a) fatigue crack initiation (marked by white arrow) and propagation areas; b) fatigue crack initiation area shown at higher magnification; c) fatigue crack striations seen on the fatigue crack propagation area.
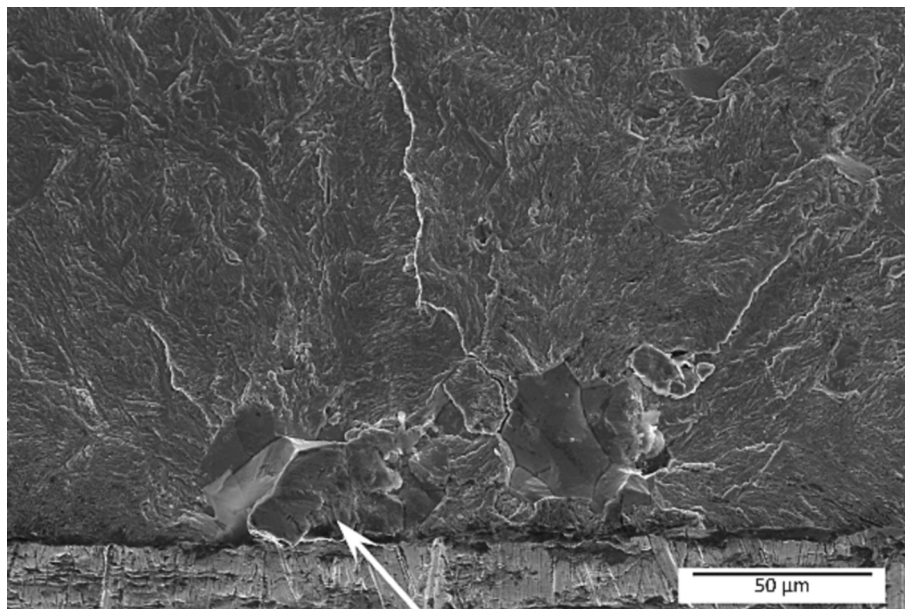
Fig. 7. SEM image of fatigue fracture surface shown by 420ma alloy tested with $\sigma_a = 300$ MPa (62619 cycles to failure): fatigue crack initiation (marked by white arrow) by intergranular cracking (the only case observed in this work).
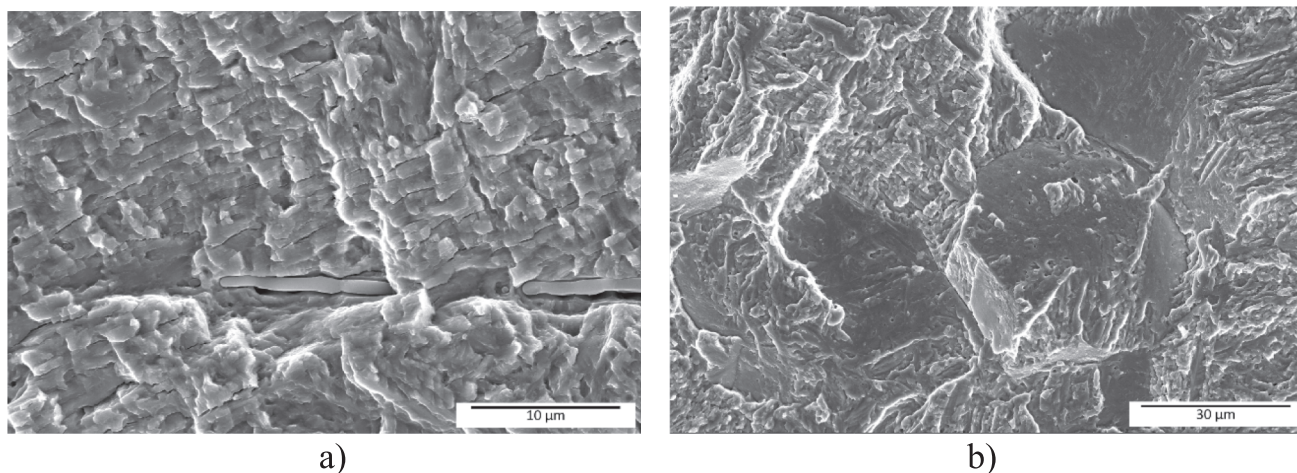
Fig. 8. SEM images of fatigue fracture surface shown by 420 alloy tested with $\sigma_a = 325$ MPa (644000 cycles to failure): a) MnS inclusion debonded from the martensitic matrix in the fatigue crack propagation area, fatigue crack striations are seen; b) local crack propagation in the intergranular mode.
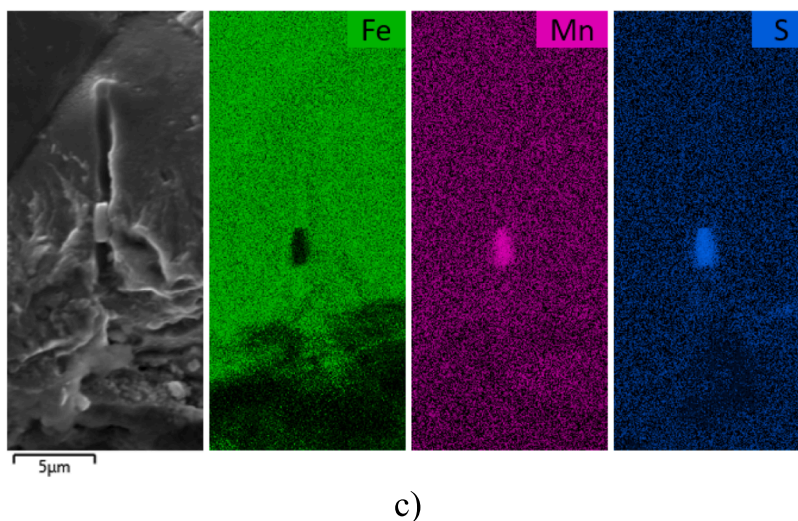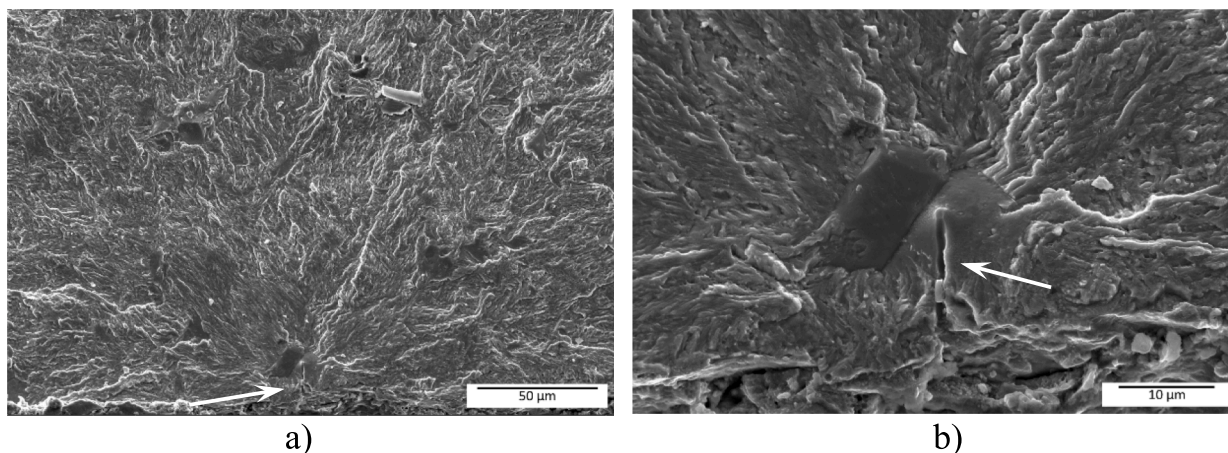
Fig. 9. SEM images of fatigue fracture surface shown by 420ma alloy tested with $\sigma_a = 460$ MPa (25804 cycles to failure): a) fatigue crack initiation (marked by white arrow) and propagation areas; b) fatigue crack initiation area shown at higher magnification (fragment of a broken MnS inclusion is seen); c) the outcomes of the EDX analysis performed on the area of fatigue crack initiation confirming the presence of MnS inclusion.

fatigue performance of the studied Q&P treated martensitic stainless steels. Nevertheless, it can be suggested that the best fatigue performance of alloy 410 is due to the interplay of several microstructural factors. First, this alloy has the largest martensite packets and blocks, leading to the lowest volume fraction of martensite packet and block boundaries acting as sites for the fatigue crack initiation (Table 4).

Second, it demonstrates the lowest volume fraction of brittle fresh martensite (Table 4). Third, it has the highest carbon content in retained austenite, promoting its mechanical stability. As it was shown in the earlier studies [17,18], steels with higher austenite stability exhibit better fatigue performance than their counterparts with lower austenite stability.

As is well known, fatigue properties strongly depend on testing conditions, including the type of loading (e.g., tensile/compressive, torsional), the testing frequency, the stress ratio applied, as well as the surface quality [40]. Even small changes in test or specimen conditions can significantly affect fatigue behaviour. The variability of fatigue testing methods and testing parameters used in the literature makes it difficult to compare the results from different studies. Nevertheless, in Table 6, the outcomes of our studies are compared with the earlier results of other authors from axial fatigue testing of martensitic stainless steels with stress ratios in the range of $R = 0...0.5$ [42–44]. A noticeable difference in the σ_f, σ_f/σ_{UTS}- and $\sigma_{max}/\sigma_{UTS}$ -values of the studied Q&P treated alloys and conventional martensitic stainless steels can be rationalized based on the above explanation. The fatigue limit and σ_f/σ_{UTS} values of the Q&P treated steels are higher compared to those of their counterparts tested with the higher stress ratio R, whereas the $\sigma_{max}/\sigma_{UTS}$-value shows an opposite trend. However, all three parameters present similar values when compared to the conventional martensitic stainless steel SS420 tested with similar R. Overall, it can be concluded that the fatigue performance of the Q&P treated martensitic stainless steels is comparable to that reported for conventional martensitic stainless steels.

4.2. Mechanisms of fatigue crack initiation and propagation in the Q&P treated martensitic stainless steels.

In the high cycle fatigue regime, the fatigue life of metallic materials is determined by fatigue crack initiation [40]. The early stage of fatigue damage in martensitic steels is characterized by the formation of slip bands acting as crack initiation sites [45,46]. Those slip bands are mainly formed along prior austenite grain boundaries, martensite packet boundaries or block boundaries [47]. Consequently, the crack initiation and crack propagation occurs often at PAGBs [48] or martensite packet and block boundaries [45]. The fatigue fracture surface analyses of our studied samples clearly show that transgranular fatigue crack initiation and propagation is dominating in the Q&P treated martensitic stainless steels (Figs. 7-9). To gain a deeper insight into fatigue crack initiation and propagation mechanisms in the Q&P treated steels, we performed EBSD mapping of both halves of the fractured 420ma sample in the corresponding regions of the fatigue crack initiation and propagation. The outcomes of the EBSD characterization showed that fatigue crack initiation and propagation occur along martensite packet or block boundaries. This is clearly demonstrated in Fig. 10 for the fatigue crack propagation area. From the EBSD maps, it is seen that the crack grows partially along martensite packet boundaries (packets are painted in different colours in Fig. 10d). In the area where the fatigue crack crosses the packet, it propagates along the block boundaries (martensite variants V are painted in different colours on Fig. 10e). In the latter case, the propagation of the fatigue crack between V18 and V18, V16 and V15, V23 and V19, V23 and V22, V18 and V17 was detected[1]. Each martensite variant in each pair belongs to different martensite blocks within the same martensite packet. These observations can be rationalized based on the incompatibility between plastic strains at the packet and block boundaries due to significant differences in the maximum Schmid factors [49,50].

*There is no noticeable transformation of retained austenite grains

---

[1] Variant numbers are according to the well-established 24 crystallographic variants of martensite crystals in the K-S orientation relationship; see, for example, [49].

into martensite in the gauge section of the fatigue tested sample. The EBSD analysis of the gauge section revealed the local volume fraction of retained austenite of 17.1 – 18.7 % similar to that measured on the Q&P treated material before testing (Table 3). However, a reduction of blocky retained austenite volume 10.8 % took place in the very thin subsurface area ($\lesssim 0.5$ μm) at the fatigue crack initiation spot, whereas the volume fraction of interlath retained austenite was not affected due to its higher mechanical stability compared to the blocky retained austenite [51]. The crack subsurface regions in the fatigue crack propagation area have a significantly reduced volume fraction of both interlath and blocky retained austenite (Table 7, Fig. 10b). The volume fraction of interlath retained austenite decreases from 2.5 % to 0.9 %, whereas the volume fraction of blocky retained austenite decreases from 16.2 % to 2.2 %. The depth of the analysed subsurface regions with significantly reduced volume fraction of retained austenite is ~ 10 μm. A comparison of the local KAM distribution histograms (Fig. 11) clearly shows that the local KAM values of the subsurface regions (e.g., areas under the crack path) are noticeably higher than those away from the crack. This indicates high density of geometrically necessary dislocations (GNDs) [52] accumulated locally under the subsurface due to the plastic zone at the tip of the propagating crack. The size of the plastic zone is determined by a range of parameters including applied global stress and crack length. Microplastic deformation within this plastic zone promotes transformation of metastable retained austenite grains into martensite. This results in the significantly reduced local volume fraction of retained austenite in the subsurface volume compared to the areas away from the crack (Table 7). Similar observations were reported earlier for a TRIP 700 steel subjected to high cycle fatigue [17] and 18CrNiMo7-6 high strength steel after fatigue crack propagation testing [53].

Although there is a body of experimental research showing intergranular fatigue crack formation and propagation in martensitic steels, the prior austenite grain boundaries play a minor role in the fatigue crack initiation and propagation of the studied materials. Generally, intergranular crack initiation is attributed to grain boundary weakening caused by precipitates or segregations. A frequently used explanation for intergranular crack initiation and early short crack propagation at prior austenite grain boundaries involves the preferential formation of carbides or segregations of impurities (such as phosphorus or sulphur) [54,55] which weakens these boundaries. The presence of hydrogen may also promote intergranular cracking in fatigue testing, especially when samples are tested at low frequencies [56]. Additionally, ferrite precipitation at prior austenite grain boundaries during rapid cooling can result in the formation of intergranular microcracking [57]. However, none of these factors took place in our studied materials. Only one sample out of the 36 demonstrated intergranular cracking on the fatigue crack initiation area (Fig. 7). This could be related to the potential local grain boundary embrittlement as a result of local nanosegregations of embrittling elements, such as phosphorus or hydrogen [58]. The surface fraction of crack growth along prior austenite grain boundaries is negligible in all analysed samples. The only secondary crack growing along prior austenite grain boundaries was detected by EBSD analysis (marked by a white arrow on Fig. 10a), and its depth was less than 10 μm.

The outcomes of our analysis are in a good agreement with the results recently presented by Okada et al. in [49]. It was shown that the vast majority of surface crack initiation and propagation in an 8Ni-0.1C martensitic steel occurred along martensite block boundaries, whereas the fraction of the fatigue cracks initiated along prior austenite grain boundaries did not exceed 4 %. Similar observations were also reported by Ueki et al. [50] for an ultralow carbon (0.0026 wt. %C) martensitic steel subjected to fatigue crack growth testing, though the authors did not observe any crack propagation along prior austenite grain boundaries in the latter work.

Fatigue fracture surface analysis performed in this study clearly shows that the MnS inclusions do not promote any fatigue crack initiation, as only one sample out of 36 presented a MnS inclusion on the

Table 6
Comparison of the fatigue limit data for martensitic stainless steels.

Material	σ_{UTS} [MPa]	Fatigue testing parameters	Fatigue limit, σ_f [MPa]	σ_f/σ_{UTS}	$\sigma_{max}/\sigma_{UTS}$	Reference
410	1276	R = 0.1	300	0.24	0.54	This work
420	1472	R = 0.1	320	0.22	0.48	This work
420ma	1451	R = 0.1	270	0.19	0.41	This work
AISI 422	880	R = 0.5, stepped loading	132.1	0.15	0.60	[42]
X4CRNIMO16-5–1	850	R = 0.5, stepped loading	151.7	0.18	0.71	[42]
A182F6NM	650	R = 0.5, stepped loading	138.9	0.21	0.85	[42]
17–4 PH	1365	R = 0.5, stepped loading	205	0.15	0.60	[42]
X20CrMoVI21	–	R = 0	~320	–	–	[43]
SS 420	1515	R = 0.1	306	0.20	0.45	[44]

a)

b)
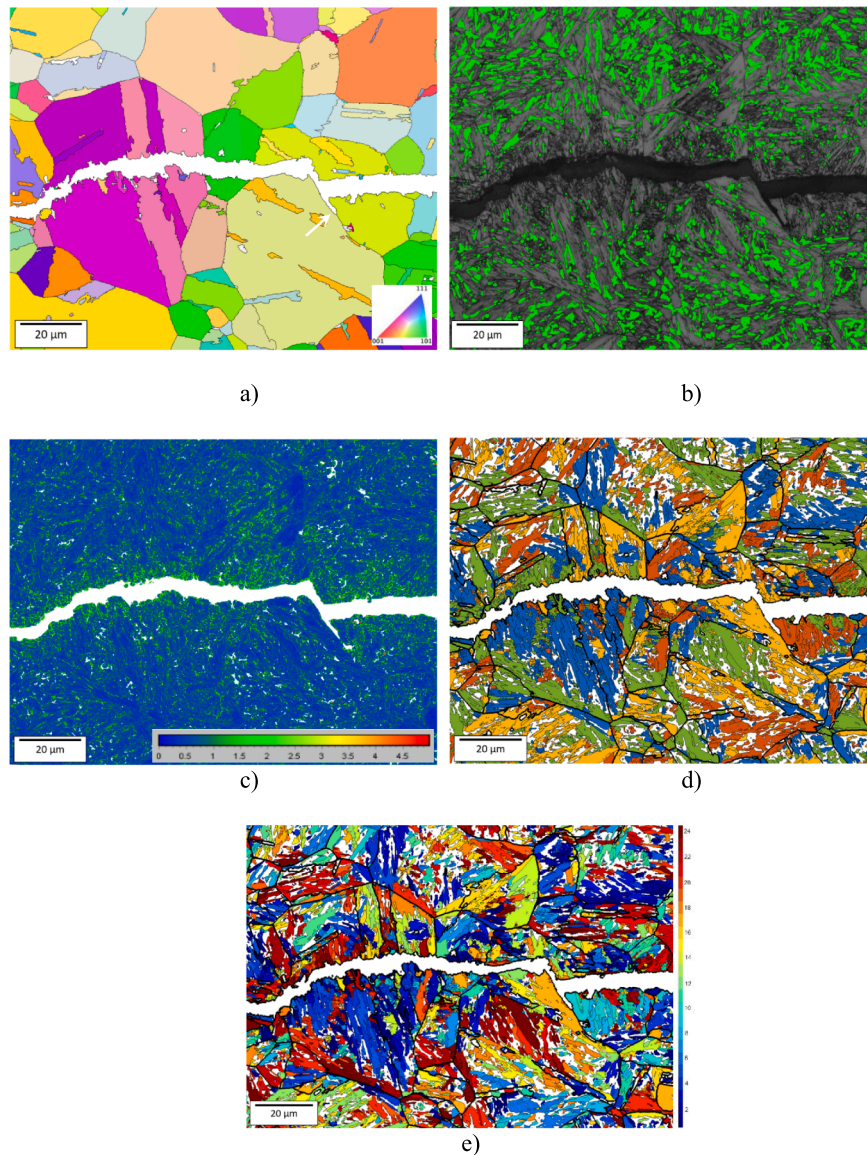
Fig. 10. Results of EBSD analysis of fatigue crack propagation area (at ~ 350 μm from the fatigue crack initiation spot) of the Q&P treated 420ma alloy: a) map of prior austenite grains, b) band contrast map with retained austenite coloured in green, c) KAM map, d) map of martensite packets, e) map of martensite variants. Black lines represent PAG boundaries along with the twin boundaries and the white arrow indicates the secondary crack along a prior austenite grain boundary. (For interpretation of the references to colour in this figure legend, the reader is referred to the web version of this article.)

c)

d)

e)

fatigue crack initiation spot (Fig. 9b,c). The analysis performed by Murakami in his book [59] showed that MnS inclusions lower fatigue strength of steels if the value of their $\sqrt{area}$ is sufficiently large. The experimental study performed by Findley and colleagues on quenched and tempered martensitic steels in [60] has shown that the allowable stress to avoid the fatigue crack initiation at the MnS inclusions dramatically increases with decreasing $\sqrt{area}$. They observed fatigue crack formation at MnS inclusions (i.e. their detrimental effect on

fatigue performance) for MnS inclusions having $\sqrt{area}$ = 10–30 μm (please see the Fig. 8 in [60]). The MnS inclusions present in our studied materials have, in average, a diameter of 0.9 μm and a length of 8.2 μm (Fig. 8a, Fig. 9). So, their cross-section area is 7.38 μm², resulting in $\sqrt{area}$ = 2.72 μm. As it was calculated in [60], the maximum allowable stress to avoid fatigue crack formation in our studied steels would be well above 2 GPa, and the MnS$\sqrt{area}$ in our materials is much smaller compared to the critical inclusion sizes leading to fatigue crack initiation

Table 7

The local volume fractions of interlath and blocky retained austenite measured on the EBSD maps taken from the areas where the fatigue crack initiation (init.) and propagation (prop.) occured in the 420ma alloy.

		Total	Interlath retained austenite (IL-RA)				Blocky retained austenite (B-RA)			
		V_{RA} [%]	V_{IL-RA} [%]	Average grain size [μm]	Min-max values [μm]	N grains	V_{B-RA} [%]	Average grain size [μm]	Min-max values [μm]	N grains
Before Fatigue	Bulk	18.7	2.5	0.56 ± 0.17	0.36–0.99	972	16.2	2.11 ± 1.44	1.00–10.39	336
After Fatigue	Init. Sub-surf.	8.2	2.8	0.41 ± 0.18	0.21–0.98	395	5.4	1.76 ± 0.70	1.02–3.69	44
	Prop. Sub-surf.	3.1	0.9	0.53 ± 0.17	0.34–0.99	308	2.2	1.7 ± 0.88	1.00–6.49	68
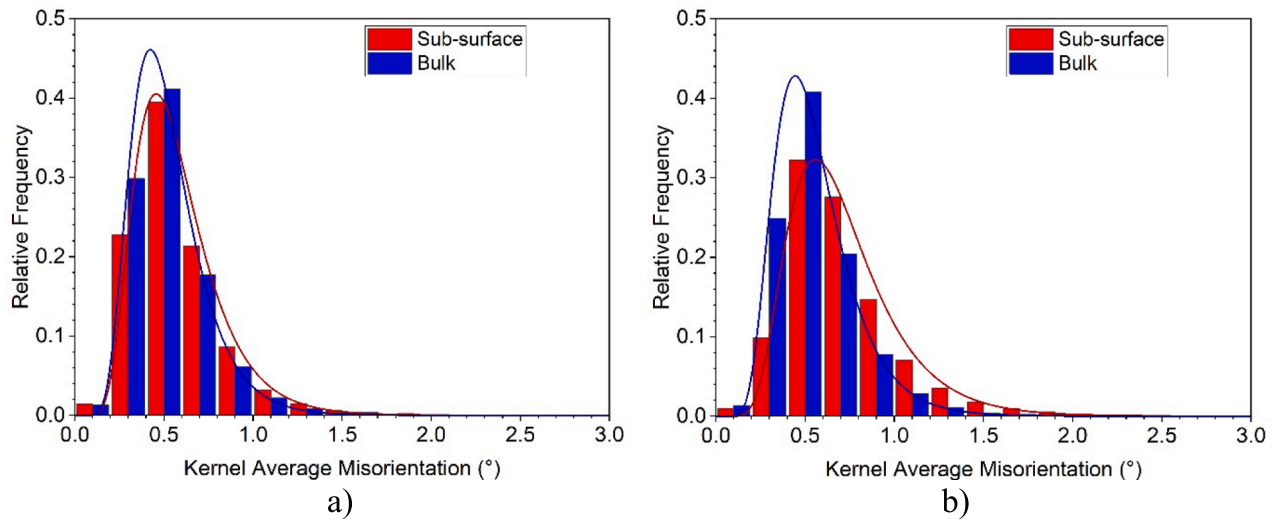
Fig. 11. Histograms of the local misorientation distribution of the Q&P treated 420ma alloy after fatigue testing with stress amplitude $\sigma_a = 460$ MPa: a) area of the fatigue crack initiation; b) area of the fatigue crack propagation (Fig. 10) at the distance of ~ 400 μm from the fatigue crack initiation area. Local misorientations of the tested sample were measured on the subsurface area (≤2 μm) from the fatigue fracture surface and the remaining area of the tested sample (bulk).

($\sqrt{area} = 10...30$ μm in [60]). Therefore, it can be concluded that the MnS inclusions in our studied steels do not affect the high cycle fatigue behaviour due to small size. Likewise, neither Fe_3C nor (Ti, Nb)C nanocarbides appear to exert a significant influence, likely due to their small size. The initiation and propagation of fatigue cracks primarily occur along martensite packet and block boundaries. In contrast, Fe_3C, (Ti, Nb)C nanocarbides are uniformly dispersed within the martensitic matrix (Fig. 4). Furthermore, although Fe_3C could be observed by SEM on fatigue fracture surfaces, it was not present on the fatigue crack initiation areas.

Debonding of MnS inclusions from the martensitic matrix during fatigue crack growth (Fig. 8a) can be related to the plastic zone at the tip of the propagating crack resulting in local failure when the local inclusion/matrix interfacial stress reaches the critical value [61]. Also, the MnS inclusions neither deviate the fatigue crack from its growth direction nor promote its bifurcation (Fig. 8a). Therefore, it can be concluded that their influence on the fatigue performance is negligible, which is in good agreement with earlier reports [62].

As is well known, the low cycle fatigue life of metallic materials is controlled by the material's resistance to fatigue crack propagation [40,63]. Our study clearly shows the transformation of retained austenite in the plastic zone during fatigue crack growth (Fig. 10b). Previous studies have shown that the enhanced volume fraction of retained austenite in Q&P treated carbon steels can noticeably improve their fatigue crack growth resistance and ΔK_{th}-value when tested with relatively low ΔK values [64]. Similarly, the retained austenite improved the low cycle fatigue life of a ferritic-martensitic steel when tested with low strain fatigue due to the energy absorption by

transformed austenite during crack propagation [65]. Therefore, it can be hypothesised that Q&P processed martensitic stainless steels may demonstrate better low cycle fatigue performance compared to their conventional counterparts. The low cycle fatigue behaviour and fatigue crack growth behaviour in the Q&P treated martensitic stainless steels are very interesting topics for further research.

5. Conclusions

The high cycle fatigue performance of novel Q&P processed martensitic stainless steels was explored. The role of their complex hierarchic microstructure in high cycle fatigue behaviour was studied. The following conclusions can be drawn based on the outcomes of this work.

Alloy chemistry significantly affects the microstructure of the Q&P treated martensitic stainless steels. The volume fraction of retained austenite tends to increase with the increasing C content (from 0.2 wt% to 0.3 wt%) and Mn content (from 0.7 wt% to 3 wt%) from 9.7 % (alloy 410) to 18.7 % (alloy 420ma). Microalloying with Nb and Ti noticeably reduces the prior austenite grain size due to the formation of complex nanoscale (Ti,Nb)C precipitates that suppress grain growth during austenitization. The average martensite packet and block size correlate with the prior austenite grain size.

Alloy 420 showed the highest fatigue limit σ_f-value (320 MPa), followed by alloy 410 (300 MPa) and alloy 420ma (270 MPa). However, the highest σ_f/σ_{UTS}-ratio is demonstrated by alloy 410 (0.24) followed by alloy 420 (0.22) and alloy 420ma (0.19). Therefore, it can be concluded that alloy 410 shows the best fatigue performance compared to other studied Q&P treated alloys. Overall, the Q&P treated

martensitic stainless steels show a satisfactory fatigue performance when compared to their conventional counterparts.

Fatigue crack initiation occurs at the surface in a transgranular mode along martensite packet or block boundaries. There is no effect of MnS inclusions and Fe_3C and complex (Ti, Nb)C nanocarbides on the fatigue crack initiation process due to their small size. The fatigue crack grows predominantly in a transgranular mode along martensite packet or block boundaries, leaving fatigue crack striations on the surface of the tested samples. The fatigue crack growth is also accompanied by debonding of the elongated MnS inclusions from the martensitic matrix.

Microplastic deformation within the plastic zone at the tip of the propagating fatigue crack leads to enhanced local KAM values and local transformation of retained austenite grains. It is hypothesized that the local TRIP effect may lead to improved low cycle fatigue performance of the Q&P treated martensitic stainless steels when compared to their conventional counterparts.

CRediT authorship contribution statement

A. Sierra-Soraluce: Conceptualization, Investigation, Formal analysis, Visualization, Writing – original draft. **G. Li:** Investigation, Formal analysis, Writing – review & editing. **M.J. Santofimia:** Supervision, Methodology, Project administration, Writing – review & editing. **J.M. Molina-Aldareguia:** Supervision, Resources, Methodology, Writing – review & editing. **A. Smith:** Supervision, Project administration, Funding acquisition, Resources, Writing – review & editing. **M. Muratori:** Resources, Investigation, Project administration, Writing – review & editing. **I. Sabirov:** Conceptualization, Methodology, Supervision, Writing – review & editing, Project administration.

Declaration of Competing Interest

The authors declare that they have no known competing financial interests or personal relationships that could have appeared to influence the work reported in this paper.

Data availability

Data will be made available on request.

Acknowledgments

References

[1] D.S. Codd, Automotive mass reduction with martensitic stainless steel, SAE International. 01 (2011) 0427.

[2] E. Pereloma, A. Gazder, I. Timokhina. Retained austenite: transformation-induced plasticity. G.E.Totten, C.Rafael (Eds.), Encyclopedia of Iron, Steel, and Their Alloys (first ed.), CRC Press (2016), pp. 3088-3103.

[3] W. Bleck, X. Guo, Y. Ma, The TRIP effect and its application in cold formable sheet steels, Steel Research International. 88 (2017) 1700218.

[4] J. Speer, D.K. Matlock, B.C. De Cooman, J.G. Schroth, Carbon partitioning into austenite after martensite transformation, Acta Materialia. 51 (2003) 2611–2622.

[5] D.V. Edmonds, K. He, F.C. Rizzo, B.C. De Cooman, D.K. Matlock, J.G. Speer, Quenching and partitioning martensite—A novel steel heat treatment, Materials Science and Engineering A. 438–440 (2006) 25–34.

[6] M. Santofimia, L. Zhao, J. Sietsma, Microstructural evolution of a low-carbon steel during application of quenching and partitioning heat treatments after partial austenitization, Metallurgical and Materials Transactions A. 40 (2009) 46.

[7] S. Kumar, S.B. Singh, Evolution of microstructure during the quenching and partitioning (Q&P) treatment, Materialia. 18 (2021), 101135.

[8] S. Kumar, Quenching and partitioning (Q&P) process: a critical review of the competing reactions, Materials Science and Technology. 38 (2022) 663–675.

[9] S. Kang, D. Pierce, D.K. Matlock, J.G. Speer, E. De Moor, Quenching and partitioning steels, Metals and Alloys. Elsevier, In Encyclopedia of Materials, 2022, pp. 84–94.

[10] T. Tsuchiyama, J. Tobata, T. Tao, N. Nakada, S. Takaki, Quenching and partitioning treatment of a low-carbon martensitic stainless steel, Materials Science and Engineering A. 532 (2012) 585–592.

[11] J. Tobata, K. Ngo-Huynh, N. Nakada, T. Tsuchiyama, S. Takaki, Role of Si in quenching and partitioning treatment of low-carbon martensitic stainless steel, ISIJ International. 52 (2012) 1377–1382.

[12] T. Koopmans, J. Sietsma, L. Zhao, M.J. Santofimia, The termal stability of quenched and partitioned steel microstructure, Steel Research International. 92 (2021) 2100290.

[13] J. Mola, B.C. De Cooman, Quenching and partitioning (Q&P) processing of martensitic stainless steels, Metallurgical and Materials Transactions A. 44 (2013) 946–966.

[14] Q. Huang, C. Schroeder, H. Biermann, O. Volkova, J. Mola, Influence of martensite fraction on tensile properties of quenched and partitioned (Q&P) martensitic stainless steels, Steel Research International. 87 (2016) 1082–1094.

[15] A. Sierra-Soraluce, G. Li, M.J. Santofimia, J.M. Molina-Aldareguia, A. Smith, M. Muratori, I. Sabirov, Effect of microstructure on tensile properties of quenched and partitioned martensitic stainless steels, Materials Science and Engineering A. 864 (2023), 144540.

[16] M. Abareshi, E. Emadoddin, Effect of retained austenite characteristics on fatigue behavior and tensile properties of transformation induced plasticity steel, Materials & Design. 32 (2011) 5099–5105.

[17] G.N. Haidemenopoulos, A.T. Kermanidis, C. Malliaros, H.H. Dickert, P. Kucharzyk, W. Bleck, On the effect of austenite stability on high cycle fatigue of TRIP 700 steel, Materials Science and Engineering A. 573 (2013) 7–11.

[18] I. Cerny, D. Mikulova, J. Sis, B. Masek, H. Jirkova, J. Malina, Fatigue properties of a low alloy 42SiCr steel heat treated by quenching and partitioning process, Procedia Engineering. 10 (2011) 3310–3315.

[19] I. de Diego-Calderón, P. Rodriguez-Calvillo, A. Lara, J.M. Molina-Aldareguia, R. H. Petrov, D. De Knijf, I. Sabirov, Effect of microstructure on fatigue behavior of advanced high strength steels produced by quenching and partitioning and the role of retained austenite, Materials Science and Engineering A. 641 (2015) 215–224.

[20] M. Thoma, G. Wagner, Effect of quenching and partitioning heat treatment on the fatigue behavior of 42SiCr steel, Metals. 11 (2021) 1699.

[21] Q. Hao, Q. Zhou, Q. Yang, K. Zhang, W. Yang, C. Zheng, C. Fu, Y. Rong, Effects of retained austenite and softened martensite on high-cycle fatigue behavior of spring steel under two loading modes, Steel Research International. 94 (2023) 2200399.

[22] X. Cheng, R. Petrov, L. Zhao, M. Janssen, Fatigue crack growth in TRIP steel under positive *R*-ratios, Engineering Fracture Mechanics. 75 (2008) 739–749.

[23] W. Liu, X. Wang, F. Guo, C. Shang, Carbides dissolution in 5Cr15MoV martensitic stainless steels and new insights into its effect on microstructure and hardness, Materials. 15 (2022) 8742.

[24] G. Solis-Bravo, M. Merwin, C.I. Garcia, Impact of precipiatate technology on the siddolution and grain-coarsening behaviour of a Ti-Nb microalloyed linepipe steel, Materials. 10 (2019) 89.

[25] M.J. Santofimia, R. Petrov, L. Zhao, J. Sietsma, Microstructural analysis of martensite constituents in quenching and partitioning steels, Materials Characterization. 92 (2014) 91–95.

[26] L. Zhao, N.H. van Dijk, E. Brück, J. Sietsma, S. van der Zwaag, Magnetic and X-ray diffraction measurements for the determination of retained austenite in TRIP steels, Materials Science and Engineering A. 313 (2001) 145–152.

[27] T. Nyyssonen, M. Isakov, P. Peura, V.T. Kuokkala, Determination of the orientation relationship between austenite and martensite from a large amount of grain pair misorientations, Metallurgical and Materials Transactions A. 47 (2016) 2587–2590.

[28] ASTM E8 / E8M-09. Standard Test Methods for Tension Testing of Metallic Materials, ASTM International.

[29] International Organization for Standardization, ISO 1099:2006(E), Metallic materials-Fatigue testing-Axial force controlled method, Geneva, Switzerland, 2006.

[30] B. He, On the factors governing austenite stability: intrinsic versus extrinsic, Materials. 13 (2020) 3440.

[31] F. Peng, Y. Xu, J. Li, X. Gu, X. Wang, Interaction of martensite and bainite transformations and its dependence on quenching temperature in intercritical quenching and partitioning steels, Materials & Design. 181 (2019), 107921.

[32] P. Xia, F. Vercruysse, C. Celada-Casero, P. Verleysen, R.H. Petrov, I. Sabirov, J. M. Molina-Aldareguia, A. Smith, B. Linke, R. Thiessen, D. Frometa, S. Parareda, A. Lara, Effect of alloying and microstructure on formability of advanced high-strength steels processed via quenching and partitioning, Materials Science and Engineering A. 831 (2022), 142217.

[33] S. Morito, H. Saito, T. Ogawa, T. Furuhara, T. Maki, Effect of austenite grain size on the morphology and crystallography of lath martensite in low carbon steels, ISIJ International. 45 (2005) 91–94.

[34] A.G. Kostryzhev, O.O. Marenych, C.R. Killmore, E.V. Pereloma, Strengthening mechanisms in thermo-mechanically processed Nb-Ti microalloyed steel, Metallurgical and Materials Transactions A. 46 (2015) 3470–3480.

[35] C. Celada-Casero, C. Kwakernaak, J. Sietsma, M.J. Santofimia, The influence of the austenite grain size on the microstructural development during quenching and partitioning processing of a low-carbon steel, Materials & Design. 178 (2019) 10784.

[36] M.J. Santofimia, L. Zhao, J. Sietsma, Model for the interaction between interface migration and carbon diffusion during annealing of martensite-austenite microstructure in steels, Scripta Materialia. 59 (2008) 159–162.

[37] D. Raabe, B. Sun, A. Kwiatkowski Da Silva, B. Gault, H.W. Yen, K. Sedighiani, P. T. Sukumar, I.R. Souza Filho, S. Katnagallu, E. Jagle, P. Kürnsteiner, N. Kusampudi, L. Stephenson, M. Herbig, C.H. Liebscher, H. Springer, S. Zaefferer, V. Shah, S. L. Wong, C. Baron, M. Diehl, F. Roters, D. Ponge, Current challenges and opportunities in microstructure-related properties of advanced high strength steels, Metallurgical and Materials Transactions A. 51 (2020) 5517–5586.

[38] Y. Wang, R. Li, X. Zuo, N. Chen, Y. Rong, The twice softening of martensitic matrix in Q-P–T steels and its effect on ductility, Heat Treatment and Surface Engineering. 1 (2019) 2–10.

[39] G.E. Dieter, Mechanical metallurgy, McGraw-Hill, New York, 1976.

[40] S. Suresh, Fatigue of Materials, Cambridge University Press, Cambridge, 1998.

[41] R.O. Ritchie, Mechanisms of fatigue crack propagation in ductile and brittle solids, International Journal of Fracture. 100 (1999) 55–83.

[42] R. De Finis, D. Palumbo, F. Ancona, U. Galietti, Fatigue limit evaluation of various martensitic stainless steels with new robust thermographic data analysis, International Journal of Fatigue. 74 (2015) 88–96.

[43] A. Atrens, W. Hoffelner, T.W. Duerig, J.E. Allison, Subsurface crack initiation in high cycle fatigue in Ti6Al4V and in a typical martensitic stainless steel, Scripta Metallurgica. 17 (1983) 601–606.

[44] C.S. Shin, T. Do, D. Lee, T.Y. So, S.H. Ko, H. Chung, P. Kwon, A comparative study on mechanical properties of fully dense 420 stainless steel parts produced by modified binder jet printing, Materials & Design. 224 (2022), 111343.

[45] K. Koschella, U. Krupp, Investigations of fatigue damage in tempered martensitic steel in the HCF regime, International Journal of Fatigue. 124 (2019) 113–122.

[46] A. Wildeis, H.-J. Christ, R. Brandt, Influence of Residual Stresses on the Crack Initiation and Short Crack Propagation in a Martensitic Spring Steel, Metals. 12 (2022) 1085.

[47] G. Seidametova, J.-B. Vogt, I.P. Serre, The early stage of fatigue crack initiation in a 12%Cr martensitic steel, International Journal of Fatigue. 106 (2017) 38–48.

[48] U. Krupp, A. Giertler, K. Koschella, Microscopic damage evolution during very-high-cycle fatigue (VHCF) of tempered martensitic steel, Fatigue & Fracture of Engineering Materials & Structures. 40 (2017) 1731–1740.

[49] K. Okada, A. Shibata, Y. Takeda, N. Tsuji, Crystallographic analysis of fatigue fracture initiation in 8Ni-0.1C martensitic steel, International Journal of Fatigue. 143 (2021), 105921.

[50] S. Ueki, T. Matsumura, Y. Mine, S. Morito, K. Takashima, Microstructural fatigue crack growth in single-packet structures of ultra-low carbon steel lath martensite, Scripta Materialia. 173 (2019) 80–85.

[51] X.C. Xiong, B. Chen, M.X. Huang, J.F. Wang, L. Wang, The effect of morphology on the stability of retained austenite in a quenched and partitioned steel, Scripta Materialia. 68 (2013) 321–324.

[52] M. Calcagnotto, D. Ponge, E. Demir, D. Raabe, Orientation gradients and geometrically necessary dislocations in ultrafine grained dual-phase steels studied by 2D and 3D EBSD, Materials Science and Engineering A. 527 (2010) 2738–2746.

[53] Y. Zhang, S. Wang, G.T. Xu, G. Wang, M.H. Zhao, Effect of microstructure on fatigue-crack propagation of 18CrNiMo7-6 high-strength steel, International Journal of Fatigue. 163 (2022), 107027.

[54] C.L. Briant, Role of carbides in tempered martensite embrittlement, Materials Science and Technology 5 (2) (1989) 138–147.

[55] R.S. Hyde, G. Krauss, D.K. Matlock, Phosphorus and Carbon Segregation Effects on Fatigue and Fracture of Gas-Carburized Modified 4320 Steel, Met. Trans. A 25 (6) (1994) 1229–1240.

[56] H. Matsumiya, A. Shibata, Y. Maegawa, K. Okada, N. Tsuji, Hydrogen-related Fatigue Fracture under Various Test Frequencies in Low-carbon Martensitic Steel, ISIJ International. 62 (2022) 2089–2094.

[57] T. Kunio, M. Shimizu, K. Yamada, M. Enomoto, A. Yoshitake, The role of prior austenite grains in fatigue crack initiation and propagation in low carbon martensite, Fatigue & Fracture of Engineering Materials & Structures. 2 (1979) 237–249.

[58] M. García-Mazarío, A.M. Lancha, M. Hernández-Mayoral, Embrittlement susceptibility induced by impurities segregation to grain boundaries in martensitic steels candidates to be used in ADS, Journal of Nuclear Materials. 360 (2007) 293–303.

[59] H. Murakami, Metal Fatigue: Effects of Small Defects and Nonmetallic Inclusions, Elsevier, 2002.

[60] K.O. Findley, R.L. Cryderman, A.B. Nissan, D.K. Matlock, The effect of inclusions on fatigue performance of steel alloys, AIST Transactions 10 (2013) 234–243.

[61] I. Sabirov, O. Kolednik, The effect of inclusion size on the local conditions for void nucleation near a crack tip in a mild steel, Scripta Materialia. 53 (2005) 1373–1378.

[62] P. Wang, P. Zhang, B. Wang, Y. Zhu, Z. Xu, Z. Zhang, Fatigue cracking criterion of high-strength steels induced by inclusions under high-cycle fatigue, Journal of Materials Science and Technology. 154 (2023) 114–128.

[63] K. Hockauf, M.F.X. Wagner, B. Mašek, T. Lampke, Mechanisms of fatigue crack propagation in a Q&P-processed steel, Materials Science and Engineering A. 754 (2019) 18–28.

[64] Z.Z. Hu, M.L. Ma, Y.Q. Liu, J.H. Liu, The effect of austenite on low cycle fatigue in three-phase steel, International Journal of Fatigue. 19 (1997) 641–646.

[65] A.F. Bower, Applied Mechanics of Solids, 1st ed., CRC Press, Boca Raton, 2009.